

Search for Dark Matter in final states with one photon and missing transverse momentum with the ATLAS experiment

F. PIAZZA

Dipartimento di Fisica, Università di Milano and INFN, Sezione di Milano - Milano, Italy

received 28 January 2021

Summary. — A search for Dark Matter is conducted in final states containing a photon and missing transverse momentum in proton-proton collisions at a centre-of-mass energy of 13 TeV. The data, collected during the period 2015–2018 by the ATLAS experiment at the CERN LHC, correspond to an integrated luminosity of 139 fb^{-1} . No deviations are observed relative to the predictions of the Standard Model and 95% confidence level (CL) upper limits, between 2.45 fb and 0.53 fb, are set on the visible cross section for contributions from physics Beyond the Standard Model, in different ranges of missing transverse momentum. The results are interpreted as exclusion limits in the models where weakly interacting Dark Matter candidates are pair-produced via an s-channel axial-vector or vector mediator. The search excludes mediators masses below 920–1470 GeV, and Dark Matter masses below 280–580 GeV at 95% CL, depending on the couplings. In addition, the results are expressed in terms of 95% CL limits on the parameters of a model with an axion-like particle produced in association with a photon.

1. – Introduction

According to astrophysical and cosmological observations, Dark Matter (DM) accounts for about 27% of the universe mass-energy. Despite compelling evidences of its existence as an invisible and gravitationally interacting component of matter, non-gravitational interactions with ordinary matter have never been confirmed and its nature and properties are still largely unknown [1].

Thanks to their potentiality to yield DM production, high energy proton-proton collisions happening at the Large Hadron Collider (LHC) at CERN can be an important instrument towards DM understanding, providing a complementary approach to DM detection with respect to direct detection and indirect detection experiments. Stable DM candidates, weakly interacting with Standard Model (SM) particles, would not decay nor interact within the detector, thus not being directly detectable. If produced in association with a SM particle, though, they can lead to the so-called $X+E_{\text{T}}^{\text{miss}}$ signature, characterized by an unbalance in the total transverse momentum of the final state,

known as missing transverse momentum (E_T^{miss}), recoiling against a visible SM particle, X (a photon γ , a jet, a W/Z boson or a Higgs boson) [2].

This report focuses on the $\gamma+E_T^{\text{miss}}$ final state, using the full Run2 dataset, collected between 2015 and 2018 by the ATLAS experiment at a centre-of-mass energy of 13 TeV and corresponding to a total integrated luminosity of 139 fb^{-1} [3]. The increased statistics, together with optimization of selection criteria and physical objects reconstruction, ensures an enhanced sensitivity of the analysis with respect to a previous publication that used a dataset of 36.2 fb^{-1} luminosity [4]. These results are part of an extensive program of DM searches at LHC, carried out within the ATLAS Collaboration. With respect to the other $X+E_T^{\text{miss}}$ searches, the $\gamma+E_T^{\text{miss}}$ final state is second in sensitivity only to the $\text{jet}+E_T^{\text{miss}}$ one and takes advantage of a cleaner final state. Results are interpreted in terms of production of two different DM candidates: WIMPs (Weakly Interacting Massive Particles) and ALPs (Axion-Like Particles).

2. – The ATLAS detector

The ATLAS experiment [5] at the LHC is a multipurpose particle detector with a forward-backward symmetric cylindrical geometry and a near 4π coverage in solid angle⁽¹⁾. It consists of an inner tracking detector surrounded by a thin superconducting solenoid providing a 2 T axial magnetic field, electromagnetic and hadron calorimeters, and a muon spectrometer. The inner tracking detector covers the pseudorapidity range $|\eta| < 2.5$. It consists of silicon pixel, silicon microstrip, and transition radiation tracking detectors. Lead/liquid-argon (LAr) sampling calorimeters provide electromagnetic (EM) energy measurements with high granularity. A steel/scintillator-tile hadron calorimeter covers the central pseudorapidity range ($|\eta| < 1.7$). The endcap and forward regions are instrumented with LAr calorimeters for both the EM and hadronic energy measurements up to $|\eta| = 4.9$. The muon spectrometer surrounds the calorimeters and is based on three large superconducting air-core toroidal magnets with eight coils each. The field integral of the toroids ranges between 2 and 6 T/m across most of the detector. The muon spectrometer includes a system of precision tracking chambers and fast detectors for triggering. A two-level trigger system is used to select events. The first-level trigger is implemented in hardware and uses a subset of the detector information to accept events at a rate below 100 kHz. This is followed by a software-based trigger that reduces the accepted event rate to 1 kHz on average depending on the data-taking conditions.

3. – Signal models

Beyond Standard Model (BSM) processes with a $\gamma+E_T^{\text{miss}}$ signature are predicted in simplified DM models of WIMPs production and in an Effective Field Theory (EFT) of ALPs production [6].

Simplified DM models proposed by the ATLAS/CMS DM Forum [7,8] predict Dirac-fermion WIMP candidates, produced through s-channel with vector or axial-vector

⁽¹⁾ ATLAS uses a right-handed coordinate system with its origin at the nominal interaction point (IP) in the centre of the detector and the z -axis along the beam pipe. The x -axis points from the IP to the centre of the LHC ring, and the y -axis points upwards. Cylindrical coordinates (r, ϕ) are used in the transverse plane, ϕ being the azimuthal angle around the z -axis. The pseudorapidity is defined in terms of the polar angle θ as $\eta = -\ln \tan(\theta/2)$. Angular distance is measured in units of $\Delta R \equiv \sqrt{(\Delta\eta)^2 + (\Delta\phi)^2}$.

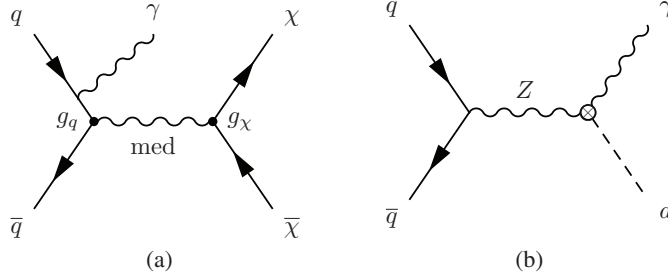


Fig. 1. – Feynman diagrams of the simplified DM model for WIMP production (a) and EFT model for ALPs production (b).

mediator, in association with a photon from Initial State Radiation (fig. 1(a)). The free parameters of these models are the DM (m_χ) and mediator (m_{med}) masses, the couplings of the mediator to the quarks (g_q), leptons (g_l) and DM (g_χ) particles, and the mediator width Γ_{med} , which is fixed to the minimal value allowed by the given choice of the couplings and of the mediator and DM masses.

ALPs, firstly introduced as a possible solution to the strong CP problem of the SM [9], can be either non-thermal DM candidates or mediators to a dark sector [10]. An EFT [6] is explored in this report (fig. 1(b)), based on an extension of the SM Lagrangian with an additional CP-odd singlet under the SM charges, arising as a (pseudo-)Nambu-Goldstone boson of a spontaneously broken symmetry at a scale f_a higher than the electroweak scale. The free parameters are the f_a scale, together with the $c_{\tilde{W}}$, one of the real operator coefficients c_i in the effective Lagrangian describing bosonic ALP couplings. The $c_{\tilde{B}}$ coefficient is fixed to $c_{\tilde{B}} = -\tan^2(\theta)c_{\tilde{W}}$, based on the assumption of null coupling to two photons, motivated by strong experimental constraints.

4. – Data and MC simulations

The analysis has been conducted on the full Run2 dataset, selecting only good quality data, acquired with stable beams conditions and in good operational status of all ATLAS detector components.

Simulated Monte Carlo (MC) samples for background processes have been generated at NLO with the Sherpa MC generator [11], while Geant4 [12] has been adopted for the full simulation of the particles interaction with the ATLAS detector [13]. The signal MC samples have been produced at NLO with the MadGraph5_aMC@NLO generator [14], in association with Pythia8 [15] for the parton shower simulation, hadronization and underlying events modelling. Both background and signal MC samples include the simulation of inelastic collisions in the same or neighbouring bunch crossing (pile-up) and are reweighted in order to reproduce the pile-up conditions observed in data. For the simplified DM models, the axial-vector scenario with $g_q = 0.25$ and $g_\chi = 1$ has been generated for masses in the transition region from on-shell to off-shell regime, and for $m_\chi = 10$ GeV and varying m_{med} . These MC samples were processed through a fast simulation of the ATLAS detector using a parameterisation of the calorimeter response and Geant4 for the inner detector and muon spectrometer. Signals with vector mediator or different couplings and other explored masses have been generated at truth level only to derive their cross section, since results for these scenarios can be obtained by cross section rescaling, being the analysis acceptance independent of the spin structure, couplings, and m_χ for fixed m_{med} in the on-shell region.

One sample for the ALPs production model, with $c_{\tilde{W}} = 1$, $m_{ALP} = 1 \text{ MeV}$, $f_a = 1 \text{ TeV}$, has been generated with fast simulation. Different masses and parameters values are explored by cross section rescaling, with a similar procedure as for simplified DM models.

Data and MC samples undergo the same event reconstruction, combining information from (real or simulated) signals in each sub-detector to describe the final state [3].

5. – Analysis strategy

The key discriminant variable is E_T^{miss} , defined as the negative vectorial sum of the transverse momenta of all the reconstructed particles (hard objects) and of the tracks matched to the primary vertex and not associated to any physics particle (soft-term) [16].

An appropriate event selection is applied to define the signal regions (SRs) of the analysis, while associated control regions (CRs) are built to derive background expectations by normalizing MC yields to data.

5.1. Event selection. – The same event selection is applied to both data and MC simulations. A trigger pre-selection requires at least one photon with $p_T > 140 \text{ GeV}$. In addition, a primary vertex must be reconstructed with at least two associated good-quality tracks, and events containing a poor-quality photon or jet arising from instrumental problems or non-collision background are removed.

The SR is defined by requiring at least one photon with $p_T > 150 \text{ GeV}$ and $\Delta\phi(\mathbf{p}_T^\gamma, \mathbf{p}_T^{\text{miss}})$, and no electrons, muons or hadronically decaying taus to reject $W/Z+\gamma/\text{jets}$ events. Up to one jet is accepted, to suppress multi-jet background, with $\Delta\phi(\mathbf{p}_T^{\text{jet}}, \mathbf{p}_T^{\text{miss}})$ to reject $\gamma+\text{jets}$ events where the E_T^{miss} arises from energy mismeasurements or misreconstruction of the photon or the jets. To further reduce the $\gamma+\text{jets}$ background, a selection cut has been optimized on the E_T^{miss} significance variable [17], providing a high discrimination power between E_T^{miss} from undetected particles and that arising from detector effects, and required to be higher than 8.5.

In order to enhance the analysis sensitivity, four inclusive SRs with increasing E_T^{miss} thresholds are defined. In addition, three exclusive SRs corresponding to different E_T^{miss} bins are introduced to allow a simplified-shape fit, as described in the following subsection. The definition of all SRs is summarized in table I. Thanks to the increased statistics, an optimization of the SRs thresholds and of the bins width have been possible, adding one more inclusive and one more exclusive SR with respect to the previously published analysis with 36.2 fb^{-1} [4].

5.2. The background estimation. – The $\gamma+E_T^{\text{miss}}$ signature can be produced by several SM processes. The dominant and only irreducible background is constituted by $\gamma+Z(\rightarrow\nu\nu)$ events, but other processes can mimic the signal final state due to detector effects. Among these, $\gamma+Z(\rightarrow\ell\ell)$ and $\gamma+W(\rightarrow\ell\nu)$ can contribute to the background

TABLE I. – Definition of the analysis Signal Regions (SRs).

	SRI1	SRI2	SRI3	SRI4	SRE1	SRE2	SRE3
$E_T^{\text{miss}}[\text{GeV}]$	> 200	> 250	> 300	> 375	$[200, 250]$	$[250, 300]$	$[300, 375]$

in case of inefficiencies in lepton reconstruction; γ +jet, if high E_T^{miss} is produced by a miscalibration or misreconstruction of a jet or a photon, or in case of wrong jet-to-primary vertex association; jets or electrons can be misidentified as photons (jet/ $e \rightarrow \gamma$ background), giving contribution to the background mainly in W/Z +jets events. Background estimation relies on the comparison between data and MC simulations for the dominant backgrounds with real photons, while data-driven techniques are employed to estimate the subleading jet/ $e \rightarrow \gamma$ background.

5.2.1. Real-photon backgrounds. Contributions from the dominant $\gamma + Z(\rightarrow \nu\nu)$ background and from $\gamma + Z(\rightarrow \ell\ell)$, $\gamma + W(\rightarrow \ell\nu)$ and γ +jets are estimated using specific CRs, defined by inverting one or more cuts of the SR, in order to enhance the contribution of each background process, while suppressing the signal. The 1-muon CR (CR1mu) for the $\gamma + W(\rightarrow \ell\nu)$ background estimation is defined by requiring exactly one muon in the event. Two CRs, the 2-muons (CR2mu) and 2-electrons (CR2el) are defined for $\gamma + Z(\rightarrow \nu\nu)$ and $\gamma + Z(\rightarrow \ell\ell)$ background, requiring exactly two muons (electrons) and vetoing the other leptons. In order to reproduce the SR kinematics in these lepton-CR, the leptons are treated as invisible particles in the E_T^{miss} calculation, by subtracting the corresponding terms. Finally, a low E_T^{miss} γ +jet CR (CRphjet) is defined with $85 \text{ GeV} < E_T^{\text{miss}} < 110 \text{ GeV}$, with an additional higher threshold $\Delta\phi(\mathbf{p}_T^\gamma, \mathbf{p}_T^{\text{miss}}) < 3.0$ to reduce possible signal contamination. The E_T^{miss} significance cut is released in all CRs.

5.2.2. Backgrounds from electron/jets misidentified as photons. The jet $\rightarrow \gamma$ background [3] estimation in each analysis region is performed through a two-dimensional sideband method (ABCD), based on the definition of three background-regions (B, C, D) enriched with events containing photons from misidentified jets. Photons in the analysis region (A) are required to satisfy identification criteria based on shower shape variables and be isolated from nearby signals in the calorimeter. The B, C and D regions are therefore obtained by reverting one or both these identification and isolation requirements.

The $e \rightarrow \gamma$ background [3] in each analysis region is estimated by scaling the event yield in specific CRs (defined in the same manner as the analysis region, but requiring an electron in place of the photon) by the probability (fake rate) for such an electron to be reconstructed as a photon. The fake rate is derived from a data sample of $Z \rightarrow ee$ events, where reconstructed photons are expected to come from misidentified electrons.

5.3. Background-only fit. – The MC predictions are normalized to data by means of a background-only maximum likelihood fit, simultaneously performed over all the CRs using the HistFitter package [18]. This fit combines inputs from all the CRs coherently, taking into account correlation of the systematic uncertainties among different regions.

The MC predictions in each SR and CR, as well as the data-driven estimates, are given in input to the likelihood as fixed parameter. The background yields for real-photon backgrounds are allowed to float in the fit through their associated normalization factors, included as free parameters in the likelihood. Finally, systematic uncertainties are treated as nuisance parameter, with Gaussian constraints. The final background yield is derived by extrapolating to the SR the normalization factors obtained from the fit in the CRs. Two fit strategies are used: the “single-bin” fit is performed separately for each inclusive E_T^{miss} bin, combining all associated CRs; the “simplified-shape fit” is performed simultaneously over all the exclusive bins and last inclusive one, providing an instrument to exploit the E_T^{miss} shape information, thus enhancing the analysis sensitivity thanks to an improved discrimination between signal and background.

6. – Results

The background-only fit is performed to derive the expected SM yields in all the SRs and CRs.

The systematic uncertainties account for both experimental and theoretical contributions [3]. The experimental systematic uncertainties are related to energy and momentum scales and resolution of the physics objects, their identification, reconstruction and isolation efficiencies, the soft-term scale and resolution and the uncertainty on the integrated luminosity measurement and pile-up reweighting. Systematic uncertainties arising from the jet/ $e \rightarrow \gamma$ background estimates are also taken into account. The theoretical uncertainties from MC simulations are related to QCD factorisation and renormalisation scales, the value of the strong coupling constants and the choice of parton distribution functions (PDFs).

After the background-only fit, the background in the first inclusive SR is composed by 63% of $\gamma + Z(\rightarrow \nu\nu)$, by 21% of jets/electrons misidentified as photons, by 13% of $\gamma + W(\rightarrow l\nu)$ and by 2% of γ +jets and by less than 1% of $\gamma + Z(\rightarrow \ell\ell)$. The E_T^{miss} distribution after the simplified-shape fit is shown in fig. 2. The data are compared to background expectations, and the distribution for three example signal samples are shown in dashed lines. In the low panel, the ratio between data and background estimation in each bin is reported. Finally, figs. 3(a) and 3(b) summarize the results of the single-bin and simplified-shape fit, respectively, in all SRs and CRs. Post-fit background expectations are compared to data. As shown in the bottom panels, reporting the significance of the discrepancies between data and background expectations, there is a good agreement in all regions, and no significant excess with respect to SM expectations in the SRs is observed.

Systematic and statistical uncertainties obtained from the fit are summarized in table II, showing that the analysis is generally dominated by statistical uncertainties.

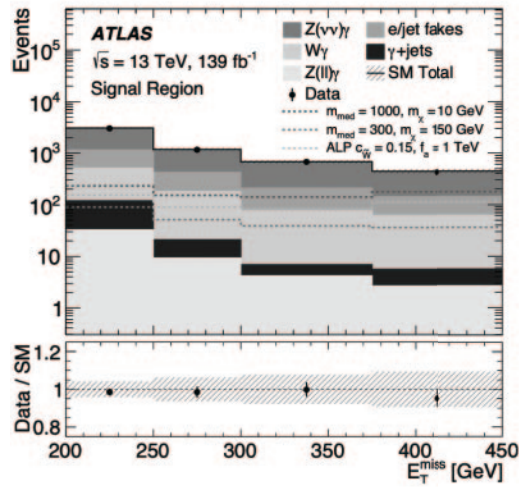


Fig. 2. – E_T^{miss} distribution for data and SM expectations after the simplified-shape fit. The low panel shows the ratio between data and background. The error bars represent data statistical uncertainty, while the dashed band the systematic and statistical background uncertainties. Three signal samples are also shown as dashed lines. Reproduced from [3].

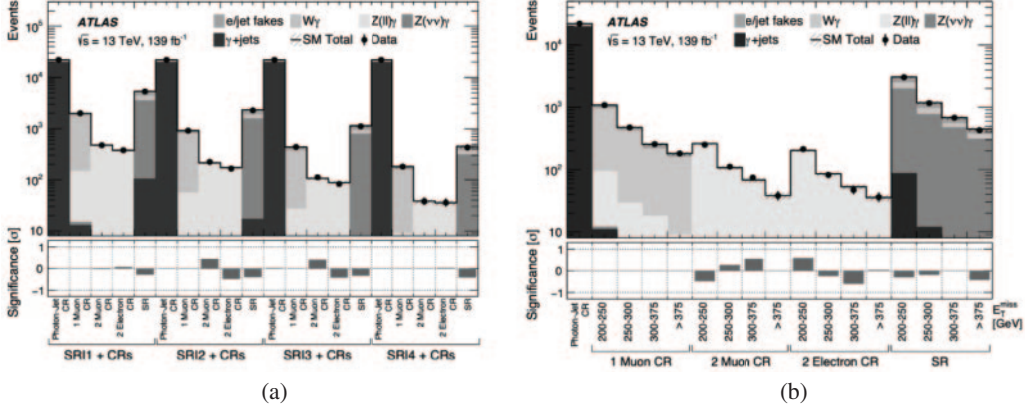


Fig. 3. – Data event yields and SM predictions from the background-only single-bin (a) and simplified-shape fit (b). Statistical and systematic uncertainties are shown. In the lower panel, the significance of the difference between data and background is shown. Reproduced from [3].

TABLE II. – *Statistical and systematic uncertainties in each SR of the analysis.*

	SRI1	SRI2	SRI3	SRI4	SRE1	SRE2	SRE3
Stat+Syst [%]	3.5	4.8	6.2	9.5	4.3	6.3	7.8
Syst [%]	2.4	3.6	5.3	8.5	3.3	5.0	6.7

From a comparison of the relative impact of each source of systematic uncertainty on the background yields, it emerges that the dominant ones come from jets (ranging from 1.4% to 4.1%) and electrons (2%–2.3%) misidentified as photons, together with jet energy scale and resolution (1.6%–2.7%). The other experimental systematics have relative impact below 1.5%, while theoretical uncertainties do not exceed 0.5%.

7. – Interpretation of the results

Results are interpreted in terms of exclusion upper limits on the simplified DM and ALPs production models, as well as model-independent limits on the visible cross section of BSM processes. The likelihood fits are based on the profile-likelihood-ratio test statistics [18] and CLs prescriptions [19].

7.1. Model-dependent limits. – A simplified-shape fit is performed on fast simulated signal samples, in both SRs and associated CRs, including the signal yields as a fixed parameter and the signal strength as freely floating normalization factor: a specific signal is excluded if the upper limit at 95% CL on its signal strength is lower than 1. Results for different parameters are obtained by cross section rescaling, as mentioned in sect. 4.

The exclusion limits for the simplified DM models are reported in the $m_{\text{med}}-m_{\chi}$ plane in fig. 4, for scenarios with axial-vector or vector mediator and different couplings to quarks and leptons. Systematic uncertainties on the signal acceptance and cross

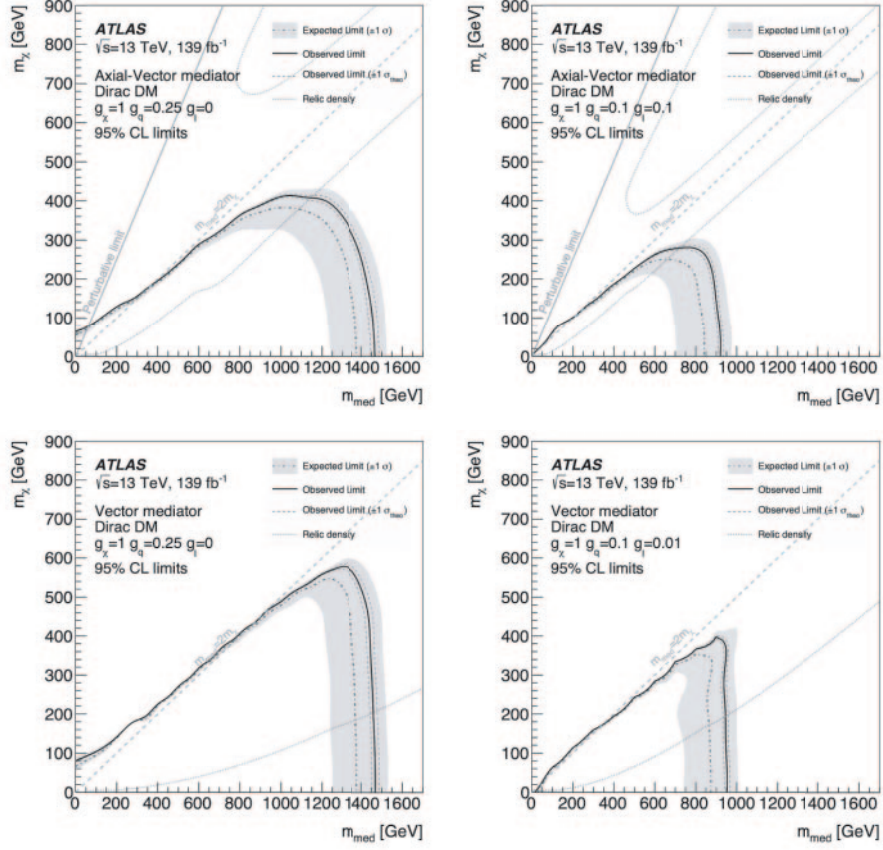


Fig. 4. – The observed (solid line) and expected (dot-dashed line) 95% CL exclusion contours in the m_χ - m_{med} plane for a simplified DM model with: axial-vector mediator and couplings $g_\chi = 1$, $g_q = 0.25$ and $g_\ell = 0$ (top left) and $g_\chi = 1$, $g_q = 0.1$ and $g_\ell = 0.1$ (top right); vector mediator and couplings $g_\chi = 1$, $g_q = 0.25$ and $g_\ell = 0$ (bottom left) and $g_\chi = 1$, $g_q = 0.1$ and $g_\ell = 0.01$ (bottom right). The area under the limit curve is excluded. The region to the left of the $m_\chi = \sqrt{\pi/2}m_{\text{med}}$ line is excluded by the perturbative limit for axial-vector mediators [20]. The area below the relic density [21] curve in the on-shell region (or above in the off-shell region in the axial-vector mediator case) corresponds to a predicted DM overabundance. Reproduced from [3].

section [3] are included, accounting for QCD factorization and renormalization scale and choice of PDFs (less than 5%), together with uncertainties in initial- and final-state radiation due to the choice of parton shower parameters (less than 10%). Only the acceptance uncertainties are included in the fit, while cross section ones are indicated as dotted lines around the observed limit. The band represents the $\pm 1\sigma$ variations including all background and signal acceptance uncertainties. The area below the contours is excluded. Depending on the couplings, the maximum excluded values are: 920–1460 GeV for m_{med} and 280–415 GeV for m_χ in the axial-vector scenario, 950–1470 GeV for m_{med} and 400–580 GeV for m_χ in the vector scenario.

The upper limits on ALPs production are shown as a function of f_a and $c_{\tilde{W}}$ in fig. 5: the limit on $c_{\tilde{W}}$ is observed to increase linearly with f_a , with $c_{\tilde{W}} > 0.12$ excluded at 95% CL for $f_a = 1$ TeV. The two bands correspond to respectively $\pm 1\sigma$ and $\pm 2\sigma$ variations,

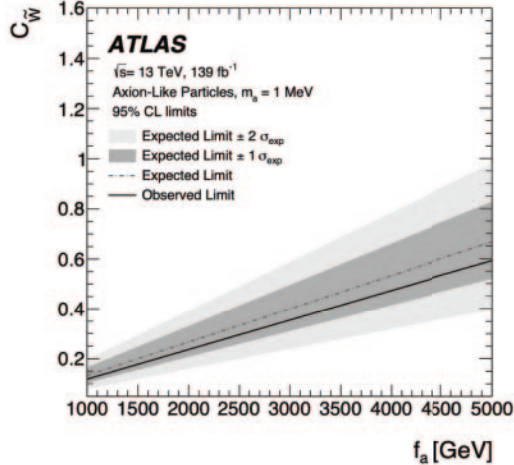


Fig. 5. – Observed (solid line) and expected (dot-dashed line) exclusions at 95% CL on the coupling $c_{\bar{V}}$ as a function of the effective scale f_a for an ALP mass of 1 MeV. The region above the limit lines is excluded. Reproduced from [3].

and a 20% theoretical uncertainty on the signal, evaluated considering the same sources of uncertainties as for the simplified DM model, is included.

7.2. Model-independent limits. – Model-independent limits on the visible cross section of new physics are provided to allow reinterpretations in terms of signal models not considered in this analysis. A profile-likelihood-ratio test is performed, based on single-bin fits in each inclusive and exclusive E_T^{miss} bin, including both SRs and CRs and enabling a signal component. The upper limits on the number of signal events can be rescaled to integrated luminosity of the dataset, providing the upper limits on the visible cross section of new physics, $\sigma \times A \times \epsilon$, where σ is the production cross section, A the fiducial acceptance (*i.e.*, the acceptance in a fiducial region defined at particle level, applying the same selection criteria as in SRs, but without accounting for detector effects) and ϵ the reconstruction or fiducial efficiency (which can be evaluated as the ratio between the particle-level and reconstruction-level acceptances). Table III reports the expected and observed limits on visible cross section, as well as the observed ones on the number of events, for each E_T^{miss} bin. The lowest reconstruction efficiency among all signals is also reported and can be used to straightforwardly derive an upper limit on the fiducial cross section, $\sigma \times A$.

8. – Conclusions

A search for an excess of events in $\gamma + E_T^{\text{miss}}$ final states with respect to SM expectation has been performed in proton-proton collisions at a centre-of-mass energy of 13 TeV, using 139 fb^{-1} of data collected by the ATLAS detector at the LHC.

Seven SRs are defined, with different E_T^{miss} selection criteria. No excess is observed, and the results are interpreted in terms of exclusion limits.

The model-independent 95% CL upper limits on the visible cross section of BSM events ranges from 2.45 to 0.53 fb, depending on the considered E_T^{miss} bin. Model-dependent 95% CL limits are set, in the $m_\chi - m_{med}$ plane, on WIMPs production in

TABLE III. – Upper limits at 95% CL on the visible cross section $\sigma \times A \times \epsilon$ (observed and expected) and on the number of events (observed), and fiducial efficiencies, ϵ . Reproduced from [3].

Signal region	$(\sigma \times A \times \epsilon)_{\text{obs}}^{95}$ [fb]	$(\sigma \times A \times \epsilon)_{\text{exp}}^{95}$ [fb]	N_{obs}^{95}	ϵ [%]
SRI1	2.45	$2.82^{+1.08}_{-0.78}$	340	76
SRI2	1.42	$1.68^{+0.63}_{-0.46}$	198	74
SRI3	0.93	$1.07^{+0.40}_{-0.29}$	129	72
SRI4	0.53	$0.63^{+0.23}_{-0.17}$	74	67
SRE1	1.80	$2.03^{+0.77}_{-0.56}$	250	75
SRE2	1.04	$1.15^{+0.43}_{-0.31}$	145	75
SRE3	0.79	$0.82^{+0.31}_{-0.22}$	109	71

simplified DM models predicting DM production via an s-channel exchange of a vector or axial-vector mediator. In the axial-vector (vector) scenario, DM candidates are excluded for masses up to 415 (580) GeV for axial-vector (vector) mediators, and mediator masses are excluded up to 1460 (1470) GeV. These results improve previous limits set using 36.2 fb^{-1} dataset. The results are also translated into limits on the $c_{\tilde{W}}$ parameter of an ALP production model, as a function of the effective scale f_a . Values of $c_{\tilde{W}} > 0.12$ are excluded at 95% CL for an ALP mass of 1 MeV and $f_a = 1 \text{ TeV}$.

REFERENCES

- [1] FREESE K., *Int. J. Mod. Phys.*, **1** (2017) 325.
- [2] GOODMAN J. *et al.*, *Phys. Rev. D*, **82** (2010) 116010, arXiv:1008.1783 [hep-ph].
- [3] ATLAS COLLABORATION (AAD G., ABBOTT B. *et al.*), *JHEP*, **02** (2021) 226, arXiv:2011.05259 [hep-ph].
- [4] ATLAS COLLABORATION, *Eur. Phys. J. C*, **77** (2017) 393, arXiv:1704.03848 [hep-ex].
- [5] ATLAS COLLABORATION, *JINST*, **3** (2008) S08003.
- [6] BRIVIO I. *et al.*, *Eur. Phys. J. C*, **77** (2017) 572, arXiv:1701.05379 [hep-ph].
- [7] ABDALLAH J. *et al.*, *Phys. Dark Universe*, **9-10** (2015) 8, arXiv:1506.03116 [hep-ph].
- [8] ABERCROMBIE D. *et al.*, *Phys. Dark Universe*, **27** (2020) 100371, arXiv:1507.00966 [hep-ex].
- [9] PECCEY R. D. and QUINN H. R., *Phys. Rev. Lett.*, **38** (1977) 1440.
- [10] BAUER M., HEILES M., NEUBERT M. and THAMM A., *Eur. Phys. J. C*, **79** (2019) 74, arXiv:1808.10323 [hep-ph].
- [11] BOTHMANN E. *et al.*, *SciPost Phys.*, **7** (2019) 034, arXiv:1905.09127 [hep-ph].
- [12] AGOSTINELLI S. *et al.*, *Nucl. Instrum. Methods A*, **506** (2003) 250.
- [13] ATLAS COLLABORATION, *Eur. Phys. J. C*, **70** (2010) 823, arXiv:1005.4568 [physics.ins-det].
- [14] ALWALL J. *et al.*, *JHEP*, **07** (2014) 079, arXiv:1405.0301 [hep-ph].
- [15] SJÖSTRAND T., MRENNA S. and SKANDS P., *Comput. Phys. Commun.*, **178** (2008) 852, arXiv:0710.3820 [hep-ph].
- [16] ATLAS COLLABORATION, *Eur. Phys. J. C*, **78** (2018) 903, 1802.08168 [hep-ex].
- [17] ATLAS COLLABORATION, ATLAS-CONF-2018-038, (2018).
- [18] BAAK M. *et al.*, *Eur. Phys. J. C*, **75** (2015) 153, arXiv:1410.1280 [hep-ex].
- [19] READ A. L., *J. Phys. G*, **28** (2002) 2693
- [20] KAHLHOEFER F., SCHMIDT-HOBERG K., SCHWETZ T. and VOGLS S., *JHEP*, **02** (2016) 016, arXiv:1510.02110 [hep-ph].
- [21] PLANCK COLLABORATION, *Astron. Astrophys.*, **594** (2016) A13, arXiv:1502.01589 [astro-ph.CO].